

Modeling of Airgap Fluxes and Performance Analysis of Five Phase Permanent Magnet Synchronous Generator for Wind Power Application

RAJA RAM KUMAR¹, (Student Member, IEEE), **SANTOSH K. SINGH¹**, (Senior Member, IEEE), **R. K. SRIVASTAVA¹**, (Senior Member, IEEE), **AKANKSHA SINGH S. VARDHAN²**, **RAJVIKRAM MADURAI ELAVARASAN³**, **R. K. SAKET¹**, (Senior Member, IEEE), **AND EKLAS HOSSAIN⁴**, (Senior Member, IEEE)

¹Department of Electrical Engineering, Indian Institute of Technology (BHU) Varanasi, Varanasi 221005, India

²Department of Electrical Engineering, Shri G.S. Institute of Technology and Science, Indore 452003, India

³Electrical and Automotive Parts Manufacturing Unit, AA Industries, Chennai 600123, India

⁴Department of Electrical Engineering and Renewable Energy, Oregon Renewable Energy Center (OREC), Oregon Institute of Technology, Klamath Falls, OR 97601, USA

Corresponding author: Rajvikram Madurai Elavarasan (rajvikram787@gmail.com)

ABSTRACT This paper proposes an Improved Magnetic Circuit (IMC) model for the optimal design and characteristics evaluation of the Five-Phase Permanent Magnet Synchronous Generator (FP-PMSG) for wind power application. Along with the Finite Element Method (FEM), the IMC model is also preferred for its faster result generation capabilities. The proposed model is used for optimal designing and performance evaluation of FP-PMSG by considering parameters such as leakage fluxes, properties of core material for rotor and stator, properties of rotor permanent magnet sleeve material, effect of saturation and armature reaction. To compute the armature reaction flux, the winding function approach has been opted. Furthermore, extensive analysis is done with respect to different sleeve and core materials along with improvising various dimensional parameters like magnet height, Magnet to Magnet (M-M) gap and sleeve length for high quality performance of FP-PMSG. To validate the results obtained from IMC model and FEM, an experimental prototype is developed and the electromagnetic performances such as generated voltage, Percentage Total Harmonic Distortion (THD) of generated voltage, terminal voltage vs load current, generated Electromotive Force (EMF) vs speed, rectified Direct Current (DC) Voltage vs DC current, output DC Power vs load resistance and percentage (%) efficiency vs current are evaluated. Through fabrication of the prototype of FP-PMSG in the laboratory, a substantial amount of engineering values have been acquired.

INDEX TERMS Five-phase, improved magnetic circuit model, modeling of airgap fluxes, permanent magnet synchronous generator, wind power.

LIST OF SYMBOLS

l_m	Length of magnet	μ_{fe}	Relative permeability of iron
δ	Gap between Magnet to Magnet (M-M)	μ_{sl}	Relative permeability of rotor sleeve
β	Half of angular length of magnet	μ_o	$4\pi \times 10^{-7}$
L	Core length of generator	μ_{pm}	Relative permeability of magnet
L_i	Iron core length	H_{pm}	Height of magnet
l_{sy}	Stator yoke length	g	Air-gap length
l_{ry}	Rotor yoke length	$g(\theta)$	Air-gap length with rotor position
l_{sl}	Thickness of rotor sleeve	g_e	Effective air-gap length
		w_e	Electrical angular speed
		r_s	Mean stator radius
		r_r	Mean rotor radius
		θ_p	Angular pole pitch

The associate editor coordinating the review of this manuscript and approving it for publication was Xue Zhou¹.

w_t	Width of the tooth
N_c	Number of turns per coil
f	frequency
θ_e	Electrical angle
$^\circ E$	Electrical degree
θ_{er}	Rotor electrical angle
k	Time harmonic
P	Poles
t	Time
θ	Mechanical rotor angle
Y	Yes
N	No

I. INTRODUCTION

Today with the increasing demand for clean energy, the use of renewable energy has become a necessity [1], [2]. Wind energy is the cleanest eco-friendly resource among all renewable energy sources [3], [4]. The Permanent Magnet Synchronous Generator (PMSG) is a suitable type for variable-speed generating system [5], [6]. It is directly connected to the turbine without any requirement of an additional gearbox [7], [8] and has several advantages like higher efficiency [9], [10], lighter rotor weight and no external excitation [11], [12]. Being a direct drive, it generates a voltage at variable wind speed and thereby, maintaining a high power factor [13]. However, it requires a full-scale converter to control the generator output voltage [14]. To reduce the size of the converter, the application of low rated switching devices in a multi-phase system poses itself as an exciting possibility [15], [16]. This system has more degree of freedom [17], offers advantages like higher reliability, fault-tolerant capability [18], [19] and high power density as compared to conventional three-phase PMSG [20], [21]. Furthermore, power density can also be improved with an optimised design. As we know that, leakage fluxes have a substantial effect on generator performances, it derates the machine by decreasing the air-gap main flux. It is an essential parameter to compute the performance and flux densities in air-gap and the magnets.

Air-gap flux distribution is a fundamental building block parameter for optimizing the design of a PMSG. Calculating the air-gap flux is somewhat difficult, as it varies with armature reaction, machine dimension parameters and core materials. Even though numerical techniques such as Finite Element Method (FEM) can precisely estimate fluxes, but they are time-consuming. Hence, an analytical model is quite often used for the quick estimation of fluxes. Permanent Magnet (PM) and winding current are two sources of flux in the PM machines. The computation of armature winding flux has been done using the winding function approach [22], whereas PM flux is calculated using its properties and dimensions.

The parameters like leakage fluxes, properties of ferromagnetic material for rotor and stator, properties of Permanent magnet sleeve, effect of saturation and armature reaction affects the accuracy of analytical model. It is a common practice that the consideration of higher degree of parameters

in the model ensures the prediction of machine performance closer to the actual values. In [23], the performance of Interior Permanent Magnet (IPM) motor has been optimised. The parameters considered in the analytical model for the performance optimization are listed in Table 1. In [24], the overhang of the IPM motor has been optimised to get the enhanced value of the flux density and EMF. The parameters considered in the analytical model for the overhang length optimization are listed in Table 1. In [25], the air-gap flux density of the permanent magnet motor is optimised so that a no-load back EMF with a lower harmonic distortion is obtained. The parameters considered in the analytical model for the air-gap flux density optimization are listed in Table 1. In [26], a detailed structure optimization of PMSG for the enhancement of the overload capability has been given. The parameters considered in the analytical model for the structure optimization are listed in Table 1. From the above discussion, it is clear that the mentioned analytical models have incorporated either the individual effect or more than two effect of the parameters namely, leakage flux, core material, permanent magnet material, rotor PM sleeve, saturation effect and armature reaction for design and performance optimization. But, the combined effects of leakage flux, core material, permanent magnet material, rotor PM sleeve, saturation effect and armature reaction is yet to be explored in the analytical model.

TABLE 1. Analytical modeling based literature.

Parameter	[23]	[24]	[25]	[26]	IMC model
Leakage flux	Y	Y	N	N	Y
Stator and rotor core material	Y	N	N	Y	Y
Rotor PM sleeve material	N	N	N	N	Y
Saturation Effect	Y	N	N	Y	Y
Armature reaction	N	N	Y	Y	Y

The following points are the prime objective of this paper:

- To propose an Improved Magnetic Circuit (IMC) model for optimal design and electromagnetic performance evaluation of FP-PMSG.
- To discuss the difficulties namely, the development of the surface mounted permanent magnet (PM) rotor with segmented PM, porous PM sleeve fixation, adjustment of the air gap and another process of developing and testing of the FP-PMSG in the laboratory.

The IMC model is capable of showing the effect of variation in dimensions and material properties in correspondence to the air-gap flux density distribution. This model is also utilised to evaluate the adverse effects due to core saturation upon the performance pertaining to variation of dimensional parameters. Besides this no-load and load tests are also performed for a better understanding of IMC model and machine behaviour. The winding function approach is opted for the computation of armature reaction flux due to five-phase winding current. Furthermore, a low-cost porous rotor sleeve is used to limit its eddy current loss.

This paper is divided in the following sections- section II discusses the generator topology and selection of material

for stator core and rotor sleeve. Section III elaborates the IMC model and electromagnetic performance parameters for the generator. Section IV compares the analytical and FEM results and considers the effect of dimensional variation on electromagnetic performances. The experimental setup and results are discussed in Section V. Finally, Section VI summarises the concluding remarks.

II. GENERATOR MODEL AND DESCRIPTION

The one fourth model of FP-PMSG is shown in Fig. 1. This Generator consists of a stator and a permanent magnet rotor. A 8 poles, 60 slots, 5 phase double-layer fractional slot windings with $72^\circ E$ phase difference between adjacent phases are placed in the stator. The winding has 12 coils per phase with 240 turns as shown in Fig.2. Coils are short-pitched by $12^\circ E$ that eliminates the higher-order harmonics in the generated voltage and also reduces conductor copper loss and sufficient weight of the machine. The different phases A, B, C, D and E are assigned the colours red, green, blue, yellow and black respectively. This winding arrangement suppresses the higher-order harmonics and reduces the copper requirement. The PMs are placed on the rotor thereby forming 8 poles. A $144^\circ E$ pole arc width is chosen by magnet short pitching to eliminate the multiple of 5^{th} order space harmonics. The short pitching of the magnets reduces its weight and cost. A rotor PM sleeve of adequate strength resists the centrifugal and inter magnetic forces and is therefore able to hold the segmented magnets at rated speed.

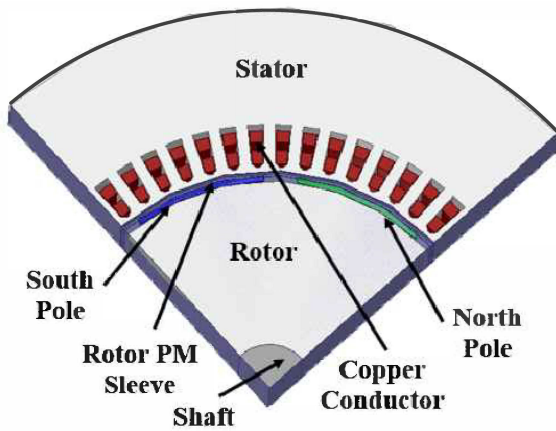


FIGURE 1. FP-PMSG Model.

A. GENERATOR TOPOLOGY

The FP-PMSG has 8 poles of magnet which are attached on the rotor surface with the help of PM sleeves. There are three flux paths, one for the main air-gap and the other two for leakage fluxes, as shown in Fig. 3. The useful flux decides the rating of the machine, whereas the leakage flux injects harmonics. There are two types of leakage fluxes namely-magnet to rotor and M-M. The M-M leakage flux can be bifurcated into two, one through air-gap and other through rotor PM sleeve. Their magnitude depends upon the material

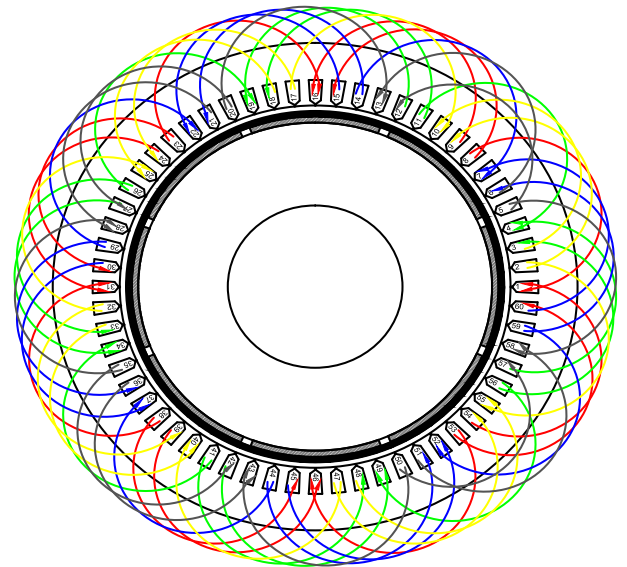


FIGURE 2. Winding pattern of FP-PMSG.

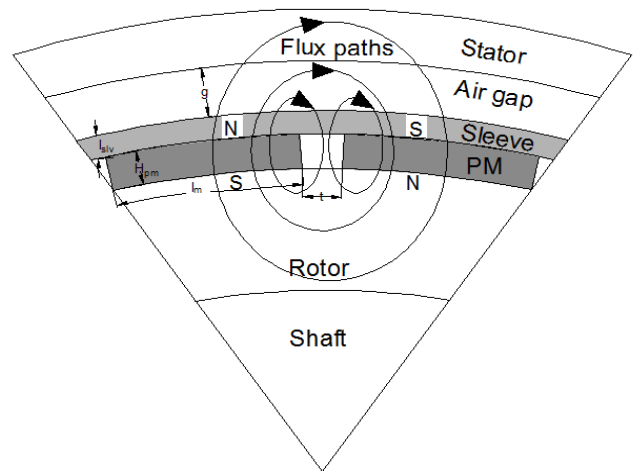


FIGURE 3. Possible flux line in FP-PMSG.

of the rotor PM sleeve. Fig.4 shows the field flux density in the machine. The plot shows that the flux density in the different parts namely rotor yoke, stator yoke and stator tooth are 0.8688 Tesla (T), 0.947 T and 1.185 T respectively. The maximum flux densities are found at the corner of PMs and the rotor surface. Its magnitude is found to be 1.264 T due to the leakage flux which ensures the optimal designing of the generator.

To meet the generator specifications, theoretical designing is done, keeping in view the saturation of core, which is further enhanced using FEM analysis. The design details and their specification are presented in Table 2 and Table 3, respectively.

B. STATOR AND ROTOR CORE MATERIAL

The stator core should have high permeability and high resistivity. Stamping of a soft magnetic alloy called dynamo grade

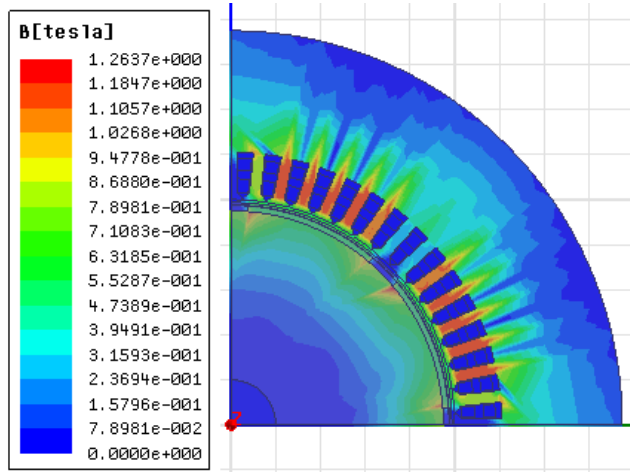


FIGURE 4. Flux Density.

TABLE 2. Design parameters.

Design parameter	Value
Radius of shaft	20 mm
Outer radius of rotor	95 mm
Height of magnet	2.5 mm
Length of air-gap	2.3 mm
Height of rotor PM sleeve	0.2 mm
Stator inner radius	100 mm
Stator outer radius	175 mm
Slot area	123.27 mm ²

TABLE 3. Machine Specification.

Parameter	Value
Power	3.423 KVA
Phase Voltage	171.18 Volt
Current	4 Amp.
Speed	400 RPM

is used to make the stator and rotor core. This material has advantages of high permeability, low coercivity and narrow hysteresis loops. The composition of iron with silicon alloy reduces the electrical conductivity, which develops smaller eddy current losses. These losses can further be reduced with the use of amorphous steel alloy for high-speed drive applications [27]. It has several advantages like very high magnetic permeability, high fracture toughness and high resistivity [28].

For high-temperature superconducting synchronous motor (HTSSM) where the field density exceeds 2 Tesla, the iron core get saturated. The iron core acts like air and may be replaced with an air core. Armature winding could also be fitted on glass fiber reinforced plastic material frame [29]. Cast iron has been considered due to its low cost irrespective of the low permeability it offers. For understanding the effect of flux distribution on performance, four core materials namely cast iron, air, amorphous steel alloy and silicon steel alloy are considered in this paper.

C. ROTOR SLEEVE MATERIAL

A durable sleeve is required to retain the segmented magnets. It counterbalances the centrifugal as well as inter M-M repulsive forces. Therefore, aluminium (Al), copper, magnetic stainless steel and carbon/glass fiber are used for this purpose. Except for carbon/glass fiber, others are easy to assemble, but they possess high electrical conductivity and cause significant eddy current loss [30]. On the other hand, carbon/glass fiber is light and robust with low electrical conductivity. However, it has less thermal conductivity and occupies a larger volume of the rotor. Despite, it is quite desirable for high-frequency application [31].

The drawback of eddy current loss in metallic sleeves could be avoided using a low cost porous metallic sleeve having similar strength. Four materials namely Al, copper, carbon fibre are considered in this paper. The permeability of the non-magnetic rotor PM sleeves (Al, copper, carbon fibre) are approximately the same but have different electrical resistivity.

III. IMC MODEL OF AIR-GAP FLUX DENSITY

The proposed IMC model of FP-PMSG is presented for computing main and leakage flux, as shown in Fig. 5. Since this machine has quarter symmetry, so only one-fourth part of the model is shown in the figure [32]. Analogous to Ohm’s law, the equivalent magnetic circuit for the IMC model is presented in Fig. 6. This network consists of two MMF sources and reluctance of various parts of the model. MMF sources are five phase winding and permanent magnets. For accurate prediction of flux distribution, this model includes reluctance of various sections of the machine- air-gap (R_g), permanent magnet (R_{pm}), stator yoke (R_{sy}), stator tooth (R_{ste}), rotor core (R_r), rotor sleeve (R_{sl}), magnet to rotor (R_{ml}), M-M through air (R_{mam}) and M-M through conducting sleeve (R_{mslm}). For different sections, the flux corresponds

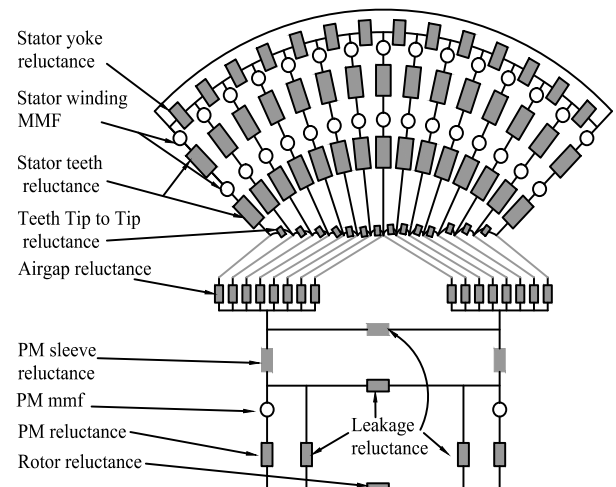
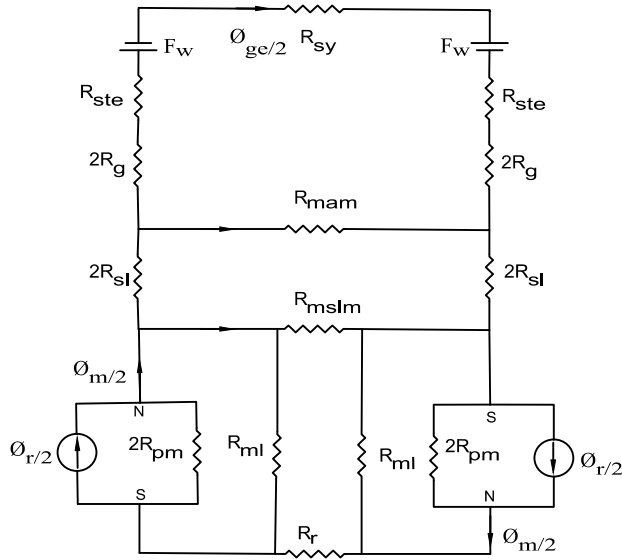


FIGURE 5. Proposed IMC model of FP-PMSG.

to air-gap (ϕ_{ge}), the surface of permanent magnet (ϕ_m), flux sources (ϕ_r), leakage magnet to rotor (ϕ_{mr}), leakage M-M via air (ϕ_{mam}) and leakage M-M through sleeve (ϕ_{mslm}) are used.



10

FIGURE 6. Improve magnetic circuit model.

All these elements are shown in Fig. 6. Since there are two MMF sources, so for the network analysis, the principle of superposition has been opted. Since PMs are the main flux source at no-load, therefore this model is used for optimization and the extraction of no-load characteristics. MMF due to armature reaction of five-phase winding is the other source which appears under loading conditions. The effect of this MMF source can be calculated separately by short-circuiting the other PM MMF sources and replacing them by their series reluctance in the network. To develop the analytical expression using IMC model for the prediction of air-gap flux density distribution, the leakage factors taken into consideration are:

$$\alpha = \frac{R_{pm}}{R_{ml}} \quad (1)$$

$$\beta = \frac{R_{pm}}{R_{mam}} \quad (2)$$

$$\gamma = \frac{R_{pm}}{R_{mslm}} \quad (3)$$

A. PERMEANCE CALCULATION FOR M-M LEAKAGE FLUX PATH

The circular arc-straight line technique is used to calculate the permeance of M-M leakage flux path [33]. In this technique flux path is divided into two curves: fringing flux is circular arc length and air-gap length between the magnets is straight line. The leakage flux has two paths, one from magnet-air-rotor, and other from magnet-air-magnet. Therefore, the two permeance are in series, which are evaluated on the basis of

their dimensions and material properties. The leakage flux between M-M through air and rotor PM sleeve is depicted in Fig. 7.

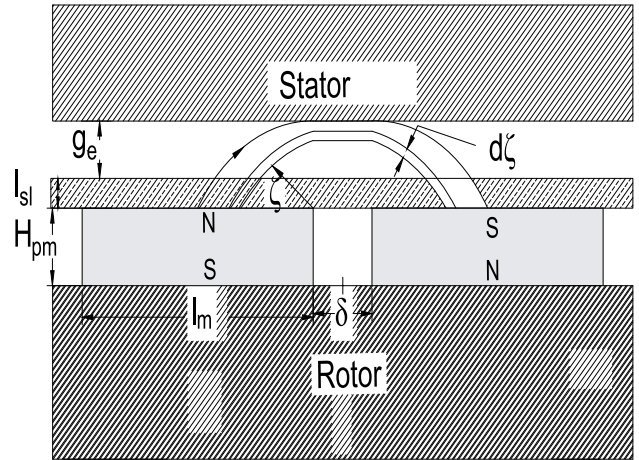


FIGURE 7. Permeance calculation for M-M leakage flux path.

Permeance of M-M leakage flux path through rotor sleeve (P_{mslm})

$$P_{mslm} = \int_0^{l_{sl}} \frac{\mu_0 \mu_{sl} L}{\delta + \pi \zeta} d\zeta = \frac{\mu_0 \mu_{sl} L}{\pi} \ln\left(1 + \frac{\pi l_{sl}}{\delta}\right) = \frac{1}{R_{mslm}} \quad (4)$$

Permeance of M-M leakage flux path through air

$$P_{mam} = \int_{l_{sl}}^{g_e} \frac{\mu_0 L}{\delta + \pi \zeta} d\zeta = \frac{\mu_0 L}{\pi} \ln\left(\frac{\delta + \pi g_e}{\delta + \pi l_{sl}}\right) = \frac{1}{R_{mam}} \quad (5)$$

B. PERMEANCE CALCULATION FOR MAGNET TO ROTOR IRON LEAKAGE PATH

The circular arc-straight line technique is used to calculate the permeance of the path of leakage flux between magnet to rotor iron as depicted in Fig. 8.

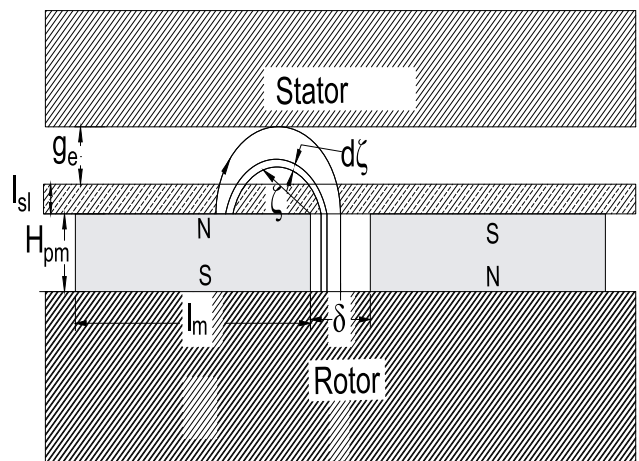


FIGURE 8. Permeance calculation for Magnet to rotor leakage flux path.

Permeance of magnet to rotor iron leakage flux path

$$P_{mi} = \int_0^{g_e} \frac{\mu_0 L}{H_{pm} + \pi \zeta} d\zeta = \frac{\mu_0 L}{\pi} \ln\left(1 + \frac{\pi g_e}{H_{pm}}\right) = \frac{1}{R_{mi}} \quad (6)$$

Leakage parameter in terms of physical dimension

$$\alpha = \frac{H_{pm}}{\pi \mu_{pm} l_m} \ln\left(1 + \frac{\pi g_e}{H_{pm}}\right) \quad (7)$$

$$\beta = \frac{H_{pm}}{\pi \mu_{pm} l_m} \ln\left(\frac{\delta + \pi g_e}{\delta + \pi l_{sl}}\right) \quad (8)$$

$$\gamma = \frac{\mu_{sl} H_{pm}}{\pi \mu_{pm} l_m} \ln\left(1 + \frac{\pi l_{sl}}{\delta}\right) \quad (9)$$

The following reduced expression are derived in terms of machine dimensions and magnetic properties.

Reluctance of Air-gap (R_g)

$$R_g = \frac{g_e}{\mu_0(l_m + 2g_e)L} \quad (10)$$

Reluctance of permanent magnet (R_{pm})

$$R_{pm} = \frac{H_{pm}}{\mu_0 \mu_{pm} l_m L} \quad (11)$$

Reluctance of stator yoke (R_{sy})

$$R_{sy} = \frac{l_{sy}}{2\pi \mu_0 \mu_{fe} r_s \theta_p L_i} \quad (12)$$

Reluctance of stator tooth (R_{ste})

$$R_{ste} = \frac{h_\delta}{\mu_0 \mu_{fe} w_t L_i} \quad (13)$$

Reluctance of rotor yoke (R_r)

$$R_r = \frac{l_{ry}}{2\pi \mu_0 \mu_{fe} r_r \theta_p L_i} \quad (14)$$

C. FLUXES UNDER NO-LOAD

Using the above mentioned reluctance parameters in the IMC model as shown in Fig. 6, under no load condition the fluxes equations are derived as followed:

Flux through the surface of permanent magnet (ϕ_m)

$$\phi_m = \frac{4R_{pm} + 2\alpha R_F(1 + 2\alpha)}{R_F(1 + 2\alpha)^2} \phi_r \quad (15)$$

where

$$R_F = R_B + 2R_C + R_r \quad (16)$$

$$R_B = \frac{R_E R_{pm}}{\gamma R_E + R_{pm}(R_{pm} + \beta R_D)} \quad (17)$$

$$R_E = R_D R_{pm} + 4R_{sl}(R_{pm} + \beta R_D) \quad (18)$$

$$R_D = R_{sy} + 4R_g + 2R_{ste} \quad (19)$$

$$R_C = \frac{2R_{pm}}{1 + 2\alpha} \quad (20)$$

Air gap flux (ϕ_g)

$$\phi_g = \frac{4R_{pm}^3}{(R_{pm} + \beta R_D)(R_{pm} + \gamma(R_A + 4R_{sl}))R_F(1 + 2\alpha)} \phi_r \quad (21)$$

where

$$R_A = \frac{R_D R_{pm}}{R_{pm} + \beta R_D} \quad (22)$$

D. MAGNETIC FLUX DENSITIES

Air gap flux density (B_g)

$$B_g = \frac{4R_{pm}^3 C_\phi}{(R_{pm} + \beta R_D)(R_{pm} + \gamma(R_A + 4R_{sl}))R_F(1 + 2\alpha)} B_r \quad (23)$$

where C_ϕ is the flux concentration factor of the air-gap. Flux density on the surface of permanent magnet (B_m)

$$B_m = \frac{4R_{pm} + 2\alpha R_F(1 + 2\alpha)}{R_F(1 + 2\alpha)^2} B_r \quad (24)$$

E. ELECTROMAGNETIC PERFORMANCE

The magnetic flux density distribution is flat-topped in the air-gap for arc-shaped magnets. This is because of odd harmonic components. (25) represents the fundamental and harmonic component of air-gap magnetic flux density distribution.

Air-gap magnetic flux density due to PM

$$B_g(\theta_{er}) = \sum_{k=1,3,5}^{\infty} B_{gk} \sin(k\theta_{er}) \quad (25)$$

where, the peak value of flux density (B_{gk}) is

$$B_{gk} = \frac{4}{\pi(\frac{\pi}{2} - \beta)} \frac{B_g}{k^2} \cos(k\beta) \sin(k\frac{\pi}{2}) \quad (26)$$

The generated electromotive force (EMF) is the rate of change of flux linkage in the winding with respect to time. In each phase winding, there are 12 short-pitched coil distributed at the periphery of stator core. The generated voltage per phase is the phasor sum of voltage generated in each of these coils. (27) is the generated voltage per phase in the machine considering fundamental and harmonics.

Induced voltage in the stator winding

$$E(t) = \sum_{k=1,3,7}^{\infty} E_k \sin(kw_e t) \quad (27)$$

where,

$$E_k = \frac{16}{P} \times 2.9563 \times N_c L_i r_s w_e B_{gk} \cos(k\frac{\pi}{30}) \quad (28)$$

F. MMF CALCULATION DUE TO FIVE PHASE WINDING

Under loading conditions there are two MMF sources as shown in Fig. 6. The MMF due to PM depends on the material properties and its dimensions which is already discussed whereas, the winding MMF which needs to be calculated. This calculation is dependent on the actual distribution of winding in slots and the phase currents. To calculate the winding MMF, the winding function approach is opted.

The winding function $N(\theta_e)$ which is given as

$$N(\theta_e) = n(\theta_e) - \langle n(\theta_e) \rangle \quad (29)$$

where, $n(\theta_e)$ and $\langle n(\theta_e) \rangle$ represents the turn function and average of turn function of the winding respectively.

Winding function can be represented as

$$N(\theta_e) = \begin{cases} \frac{22}{15}N_c & 0 \leq \theta_e \leq \frac{168\pi}{180}; \\ \frac{-8}{15}N_c & \frac{168\pi}{180} \leq \theta_e \leq \frac{192\pi}{180}; \\ \frac{-23}{15}N_c & \frac{192\pi}{180} \leq \theta_e \leq \frac{336\pi}{180}; \\ \frac{-8}{15}N_c & \frac{336\pi}{180} \leq \theta_e \leq 2\pi; . \end{cases} \quad (30)$$

For five phase winding, the winding functions are $N_a(\theta_e)$, $N_b(\theta_e)$, $N_c(\theta_e)$, $N_d(\theta_e)$ and $N_e(\theta_e)$ for phases A, B, C, D and E respectively. This can be represented as

$$\begin{aligned} N_a(\theta_e) &= \sum_{h=1,2,3,..}^{\infty} A_h \cosh(\theta_e - \theta_{wd}) \\ N_b(\theta_e) &= \sum_{h=1,2,3,..}^{\infty} A_h \cosh(\theta_e - \theta_{wd} - \frac{2\pi}{5}) \\ N_c(\theta_e) &= \sum_{h=1,2,3,..}^{\infty} A_h \cosh(\theta_e - \theta_{wd} - \frac{4\pi}{5}) \\ N_d(\theta_e) &= \sum_{h=1,2,3,..}^{\infty} A_h \cosh(\theta_e - \theta_{wd} - \frac{6\pi}{5}) \\ N_e(\theta_e) &= \sum_{h=1,2,3,..}^{\infty} A_h \cosh(\theta_e - \theta_{wd} - \frac{8\pi}{5}) \end{aligned} \quad (31)$$

where

$$\begin{aligned} A_h &= \frac{2N_c}{\pi \cdot h} [2 \sinh(\frac{7\pi}{15}) + \sinh(\frac{9\pi}{15})] \\ \theta_{wd} &= \frac{7\pi}{15} \end{aligned} \quad (32)$$

Phase current are $I_a(\omega_e t)$, $I_b(\omega_e t)$, $I_c(\omega_e t)$, $I_d(\omega_e t)$ and $I_e(\omega_e t)$ for phases A, B, C, D and E respectively. This can be represented as

$$\begin{aligned} I_a(\omega_e t) &= \sum_{k=1,3,7,..}^{\infty} I_k \cos k(\omega_e t - \theta_d) \\ I_b(\omega_e t) &= \sum_{k=1,3,7,..}^{\infty} I_k \cos k(\omega_e t - \theta_d - \frac{2\pi}{5}) \\ I_c(\omega_e t) &= \sum_{k=1,3,7,..}^{\infty} I_k \cos k(\omega_e t - \theta_d - \frac{4\pi}{5}) \\ I_d(\omega_e t) &= \sum_{k=1,3,7,..}^{\infty} I_k \cos k(\omega_e t - \theta_d - \frac{6\pi}{5}) \\ I_e(\omega_e t) &= \sum_{k=1,3,7,..}^{\infty} I_k \cos k(\omega_e t - \theta_d - \frac{8\pi}{5}) \end{aligned} \quad (33)$$

Where I_k is the peak current and θ_d is the phase shift between the voltage and current.

MMF due to five phase winding (F_{ar}) can be calculated as

$$\begin{aligned} F_{ar}(\theta_e, \omega_e t) &= N_a(\theta_e)I_a(\omega_e t) + N_b(\theta_e)I_b(\omega_e t) \\ &+ N_c(\theta_e)I_c(\omega_e t) + N_d(\theta_e)I_d(\omega_e t) + N_e(\theta_e)I_e(\omega_e t) \end{aligned} \quad (34)$$

From the above equation, MMF due to five phase winding (F_{ar}) can be written as

$$\begin{aligned} F_{ar}(\theta_e, \omega_e t) &= \sum_{h=1,2,3,..}^{\infty} \sum_{k=1,3,7,..}^{\infty} \frac{A_h I_k}{2} [(1 + 4 * (-1)^{h+k} \\ &\cos(h+k) \frac{2\pi}{5} \cos(h+k) \frac{\pi}{5}) (\cos(h\theta_e + k\omega_e t - h\theta_{wd} - k\theta_d)) \\ &+ (1 + 4 * (-1)^{h-k} \cos(h-k) \frac{2\pi}{5} \cos(h-k) \frac{\pi}{5}) \\ &(\cos(h\theta_e - k\omega_e t - h\theta_{wd} + k\theta_d))] \end{aligned} \quad (35)$$

MMF due to five phase winding (F_{ar}) can be rewritten as

$$F_{ar}(\theta_e, \omega_e t) = \sum_{h=1,2,3,..}^{\infty} \sum_{k=1,3,7,..}^{\infty} F_{ar}(h\pm k) \cos(h\theta_e \pm k\omega_e t - h\theta_{wd} \mp k\theta_d) \quad (36)$$

MMF due to armature reaction (F_w) in the network can be given as

$$F_w = \frac{\sum_{h=1,2,3,..}^{\infty} \sum_{k=1,3,7,..}^{\infty} F_{ar}(h\pm k)}{2} \quad (37)$$

G. FLUX AND MAGNETIC FIELD DENSITY DUE TO ARMATURE REACTION

The flux due to armature reaction is found using the IMC model shown in Fig. 6. This network has only five phase winding MMF sources and reluctance of various parts of the machine.

The air-gap flux (ϕ_{gar}) due to armature reaction can be given as

$$\phi_{gar} = \frac{4F_m(R_{pm}R_H + 4R_{sl}\beta\gamma(1 + 2\alpha)R_r)}{R_{pm}R_G + R_D(R_{pm}R_H + 4R_{sl}\beta\gamma(1 + 2\alpha)R_r)} \quad (38)$$

where

$$\begin{aligned} R_G &= (1 + 2\alpha)(R_{pm}4R_{sl} + R_{pm}R_r + 4R_{sl}R_r) \\ &+ 4R_{pm}(R_{pm} + 4R_{sl}\gamma) \\ R_H &= (1 + 2\alpha)(2R_{pm} + \gamma R_r + \beta(R_{sl} + R_r)) \\ &+ 4R_{pm}(\gamma + \beta) + 16\beta\gamma R_{sl} \end{aligned} \quad (39)$$

Using (38), the air-gap flux density (B_{ar}) due to armature reaction can be found out.

IV. RESULTS AND MODEL VERIFICATION

The flux distribution in the air-gap depends on the dimensional parameters, material properties and armature reaction. The armature reaction flux has less significance than PM flux, so the design optimisation is carried out under no-load condition. The dimensions which directly affect flux distribution includes height of magnet, M-M gap and width of rotor

PM sleeve. For an optimum magnet design, it is required to vary these parameters keeping the dimensions fixed for the machine. In addition, proper selection of material eliminates the non-linear behaviour of core and also reduces the space harmonics. For this, different core and rotor sleeve material are considered to realise their effect on the distribution of air-gap flux. Furthermore, steel M400-50A is also considered for the realization of adverse effect of saturation. In this context, IMC model is proposed which calculates the air-gap flux density distribution. (23) and (24) are used to compute the air-gap magnetic flux density and the surface of the magnet under no-load respectively. (27) presents the effect on generated voltage. Under loading condition the effect of armature reaction on air-gap magnetic flux density and performance is also carried out. The analytical results of IMC model is verified with FEM results in this section.

A. VARIATION OF STATOR AND ROTOR CORE MATERIAL

The flux distribution is directly associated with the core material, as shown in Table 4. It is found that as the core material varies from air to amorphous steel, the air-gap flux density is increased by 118.177%. Similarly, for Cast iron and Silicon steel, it is increased to 115.67% and 118.15% with respect to air. The FEM for B_g is higher than analytical by 2.443%. As compared to air core, the flux density at the surface of the magnet is increased by 100.3%, 98.179% and 100.286% for amorphous steel, cast iron and silicon steel respectively. The FEM result for B_m is higher by 2.029% to that of analytical results. Among these materials, amorphous steel has a maximum B_g and B_m because of high permeability. It has lower conductivity and hence reduced iron loss.

TABLE 4. Variation of stator and rotor core material.

Parameter	Analytical		FEM	
	B_g	B_m	B_g	B_m
Core materials				
Silicon steel alloy	0.56207	0.63798	0.56937	0.64528
Cast iron	0.55568	0.63127	0.56300	0.63840
Air	0.25765	0.31854	0.26410	0.32500
Amorphous steel alloy	0.56213	0.63804	0.56943	0.64534

B. VARIATION OF ROTOR PM SLEEVE MATERIAL

The variation of rotor PM sleeve material is enlisted in Table 5. It is observed that, there is no variation in the air-gap flux density and the flux density at the surface of permanent magnets because of non-magnetic rotor PM sleeve- Al, copper, carbon fiber. However, for Al the FEM results of B_g and B_m are found to be respectively, 1.302% and 1.144% higher than predicted results. For stainless steel, the B_g and B_m are increased by 4.47% and 3.92% respectively. Among these materials, magnetic silicon steel has maximum B_g and B_m because of high permeability, but it provides the lowest reluctance path for leakage flux which enhances the local fluxes in the PMs, leads to demagnetization effect in it. Because of that, it is avoided in general practice as a sleeve. The carbon fibre is an effective solution with lower conductivity but occupies larger rotor volume.

TABLE 5. Variation of rotor sleeve materials.

Parameter	Analytical		FEM	
	B_g	B_m	B_g	B_m
Rotor sleeve material				
Stainless steel	0.58582	0.66301	0.59252	0.66970
Al	0.56208	0.63798	0.56938	0.64528
Copper	0.56208	0.63798	0.56938	0.64528
Carbon fiber	0.56208	0.63798	0.56938	0.64528

C. VARIATION OF HEIGHT OF PERMANENT MAGNET

For this analysis, M400-50A steel alloy is used as the core, and an Al with 0.2 mm width is used a rotor PM sleeve. The M-M gap is 9° , and inner and outer radius of stator and rotor is kept fixed. With the magnet height being increased, the length of the air-gap decreases, which enhances the air gap flux. With the saturation of the core material the permeability of the actual machine varies and this variation is more significant for the stator teeth. From Table 6, the height of magnet varies from 1 mm to 2.5 mm, the B_g and B_m are increased linearly by 152.97% and 121.91% respectively with respect to 1 mm magnet. As a result of stator teeth saturation, non linearity increases. In case of NdFeB when the magnet height is increased from 2.5 to 3.5 mm, maximum flux density in the air-gap is found to be 0.6585 Tesla at 3.5 mm. As we go beyond 3.5 mm till 4.5 mm, flux density starts to decrease in the air-gap. The analytical and FEM results for NdFeB are reviewed and are in close agreement.

In Fig. 9, the generated voltage of different height of magnet has been reported. Since, the generated voltage is directly associated with the air-gap flux density, so the effect of saturation is appeared in the generated voltage. Similarly, Fig. 10 shows a better visualization of the adverse effect of saturation on the no-load performance under varying PM dimensions. It also shows that, the FEM and analytical results are in good agreement under the saturation condition because proper care has been taken for their material property.

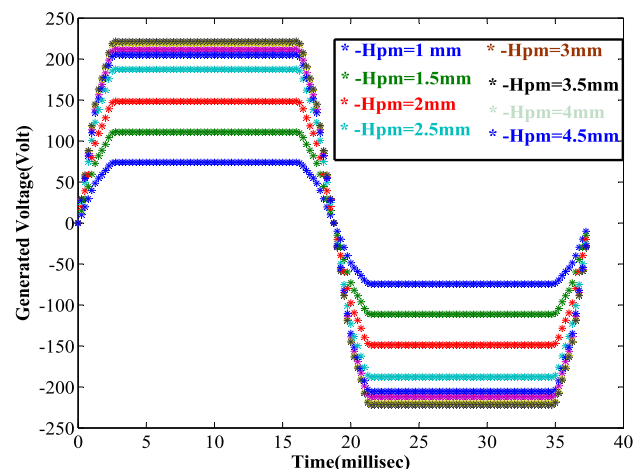


FIGURE 9. Generated Voltage for the variation of magnet height (1 mm to 4.5 mm).

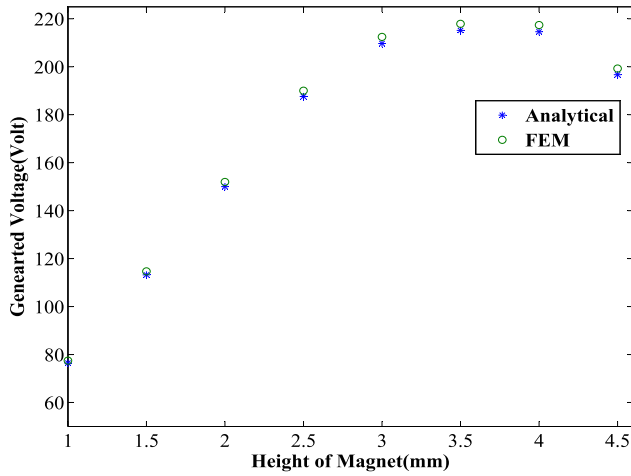


FIGURE 10. Generated Voltage with saturation for the variation of magnet height (1 mm to 4.5 mm).

TABLE 6. Variation of permanent magnet height.

Parameter		Analytical		FEM	
H_{pm} (mm)	g_e (mm)	B_g	B_m	B_g	B_m
1.0	3.8	0.22222	0.28750	0.22510	0.29370
1.5	3.3	0.33310	0.40920	0.33670	0.41560
2.0	2.8	0.44490	0.52490	0.45050	0.53120
2.5	2.3	0.56210	0.63800	0.56940	0.64530
3.0	1.8	0.63500	0.71223	0.64320	0.71945
3.5	1.3	0.65850	0.73675	0.66690	0.74621
4.0	0.8	0.65680	0.72940	0.66540	0.73889
4.5	0.3	0.61510	0.69039	0.62290	0.69748

D. VARIATION OF ROTOR PM ALUMINIUM SLEEVE THICKNESS

The flux density is affected by the rotor PM aluminium sleeve thickness as shown in Table 7. For this analysis, silicon steel material as core, magnet of height 2.5 mm and M-M gap of 9° are used. The dimensional parameter of inner and outer radius of stator and rotor are also kept fixed. As the width of sleeve thickness varies from 0.1mm to 1.0mm, the B_g is increased by 2.14% and the B_m is decreased by 2.079%. The simulated FEM results for B_g and B_m for 0.1 mm of sleeve thickness are 1.159% and 1.078% higher than predicted results.

TABLE 7. Variation of rotor sleeve thickness.

Parameter		Analytical		FEM	
l_{sl} (mm)	g_e (mm)	B_g	B_m	B_g	B_m
0.1	2.4	0.5608	0.6397	0.5673	0.6466
0.2	2.3	0.5621	0.6380	0.5680	0.6450
0.3	2.2	0.5634	0.6363	0.5740	0.6427
0.4	2.1	0.5647	0.6348	0.5710	0.6416
0.5	2.0	0.5660	0.6333	0.5720	0.6400
0.6	1.9	0.5673	0.6318	0.5749	0.6383
0.7	1.8	0.5687	0.6304	0.5758	0.6373
0.8	1.7	0.5700	0.6290	0.5763	0.6351
0.9	1.6	0.5714	0.6277	0.5782	0.6233
1.0	1.5	0.5728	0.6264	0.5787	0.6335

In Fig. 11 the generated voltage of different rotor PM sleeve thickness has been reported. From this plot, it is found that the generated voltage due to variation of sleeve thickness, from 0.1 mm to 1 mm is increased by 2.191%.

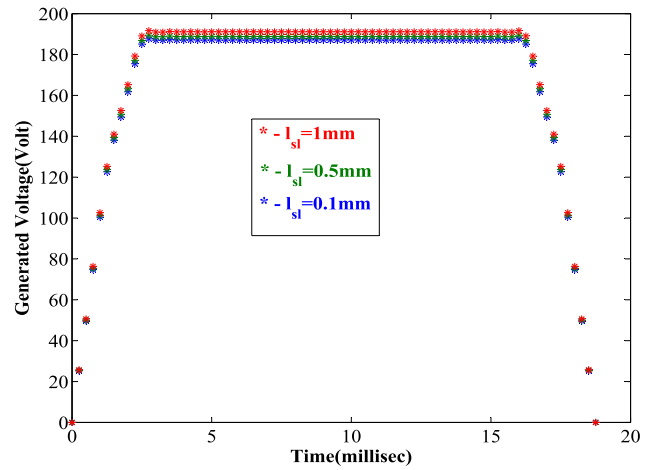


FIGURE 11. Variation of rotor sleeve thickness(0.1 mm to 1 mm).

E. VARIATION OF M-M GAP

The distribution of flux is slightly affected by the M-M gap as given in Table 8. For this analysis, the core and PM sleeve are made of silicon steel alloy and Al (0.2 mm) respectively. The height of the magnet is 2.5mm, and inner and outer radius of stator and rotor remains unchanged. As the M-M gap increases, the flux in the air-gap decreases. The M-M gap is varied from 5.105 mm to 15.32 mm. It is observed that the B_g and B_m are decreased by 393.65% and increased by 285.739% respectively. The simulated FEM results for B_g and B_m for 5.105mm of M-M gap are 0.972% and 0.967% higher than calculated results. The generated voltage is decreased by 6.13% as shown in Fig. 12. On the other hand, the cogging torque also gets affected due to M- M gap, i.e. as the M-M gap increases the cogging torque decreases abruptly. It is because, cogging torque is directly proportional to square of the air gap flux.

TABLE 8. Variation of length of permanent magnet.

Parameter	Analytical		FEM	
	B_g	B_m	B_g	B_m
5.105	0.5967	0.5996	0.6025	0.6054
6.807	0.5949	0.6021	0.6013	0.6077
8.508	0.5893	0.6084	0.5951	0.6148
10.21	0.5831	0.6151	0.5887	0.6215
11.91	0.5765	0.6224	0.5825	0.6282
13.61	0.5695	0.6300	0.5759	0.6368
15.32	0.5621	0.6380	0.5694	0.6453

F. IMPACT OF ARMATURE REACTION ON THE MAGNETIC FIELD DISTRIBUTION

The air-gap flux (ϕ_{ge}) under loading condition can be computed using IMC model shown in Fig. 6. Since this network consists of two MMF sources, therefore the air-gap flux is the resultant of no-load flux (ϕ_g) due to PMs and the armature reaction flux (ϕ_{ar}) due to five-phase winding. The no-load flux and armature fluxes are computed using (21) and (38) respectively. The air-gap flux density at no-load is found 0.5621T whereas, 0.0841T due to armature reaction.

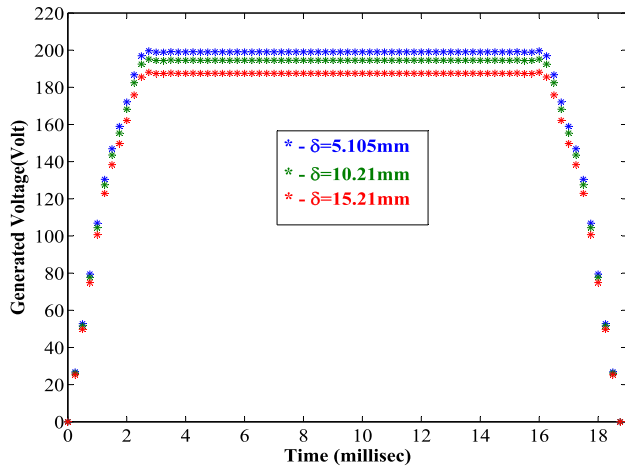


FIGURE 12. Variation of M-M gap(5.105 mm to 15.32 mm).

The flux density is also carried out using FEM in which the no-load flux density is found 0.5694T, whereas 0.0839T due to five-phase winding excitation. The analytical results are found in good agreement with FEM result.

V. EXPERIMENTAL SET-UP AND RESULTS

The fabricated prototype for the FP-PMSG, is shown in Fig. 13. It consists of three main parts, namely, stator, adjustable-clamp fitted in iron frame and rotor. The stator core is made up of silicon steel stamping and it has 60 slots and 5 phase balanced distributed double layer winding in it. There are 240 turns in each phase, that is distributed in 24 slots on the periphery of the stator. Each slots has two coil-side in it and each coil has a span of 7 slot pitch. Suppose, if one coil side is present in slot 1, then the other coil side is present in slot 8 and this process of winding is shown in Fig. 14 and Fig. 15. Using the LCR meter, the value of per phase winding resistance and inductance are measured as 5.02 ohm and 35.42 milli henry respectively.

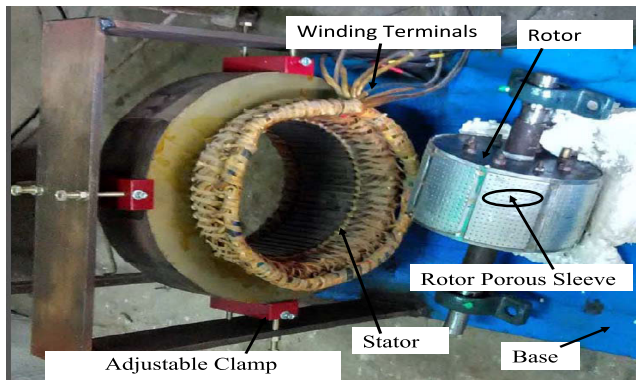


FIGURE 13. Stator and rotor of developed generator.

The rotor consists of 8 magnets, placed mutually 45° apart which are 80% of the pole pitch. In order to reduce the PM eddy current losses, the segmented magnets of size 6.4 mm x 6.4 mm x 2.5 mm are used, as shown in Fig. 16. In segmented



FIGURE 14. Stator winding intermediate process.



FIGURE 15. Stator with complete winding.



FIGURE 16. Magnet Pasting Process.

magnets, same nature of small magnets are pasted together. While pasting same nature of magnets, a large inter M-M force is developed due to which pasting becomes difficult. Hence, for pasting the magnets firmly, a non magnetic screw fitted frame is used. This frame is made up of aluminium and the screw in it is made up of brass, to avoid attraction between magnet and the frame. The screw of the frame holds

the segmented magnets for a certain period of time, so that the adhesives which are used for pasting magnet, should be able to overcome the M-M repulsive forces.

A rotor PM sleeves is also used in addition to adhesives, to ensure pasting of the magnets firmly on the rotor surface. An aluminium porous sleeves of thickness 0.2 mm is used for this purpose, as it is cheaper and easy to mount on the surface of PM on the rotor. There are 160 holes of 1 mm diameter present in the porous rotor PM sleeve.

The eddy current losses in rotor sleeve is directly proportional to the height and effective area, whereas stress is inversely proportional to the area of the sleeve. As a result, porous sleeve limits the generation of eddy current losses whereas, the stress get increased compared to conventional sleeve. The porous rotor PM sleeve has negligible effect on both no-load and loaded conditions on the electromagnetic performances. Using mechanical adjustable-clamp support, the air-gap length of 2.3 mm is provided for the protection of magnet against armature reaction during the short circuit condition of the winding. The experimental setup to observe the variation of the magnitude of flux density as a function of air-gap is shown in Fig. 17. For testing the polarity of magnets, digital gauss meter (model no.:DGM-102) is used which indicates north pole by showing the magnitude of B-field in gauss, and for the south pole Negative value of B-field is displayed in gauss-meter.

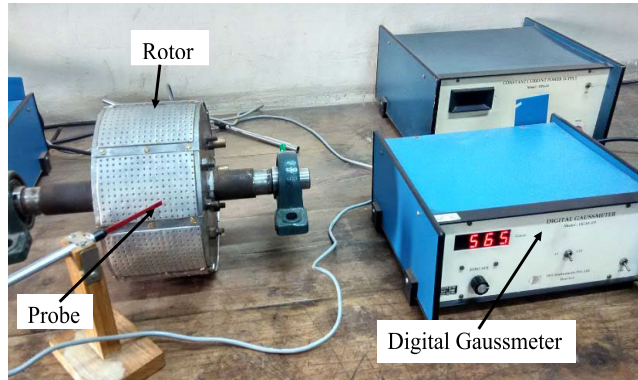


FIGURE 17. Polarity test of rotor for developed generator.

The experimental test-rig for the developed FP-PMSG is shown in Fig. 18. It is found that at 384.59 rpm the generated voltage is 186.45 volts at 25.64 Hz and the rectified DC voltage is 373 volts as shown in Fig. 19. The voltage generated by the machine at 400 rpm is utilised for validating analytical and simulated results. The experimental findings have been found to be in strong agreement, as shown in Fig. 20. The generated voltage from analytical and simulated FEM results are respectively, 3.28% and 2.02% lesser than the experimental result at the rated speed of 400 rpm. These values are enlisted in Table 9. In Fig.21, FFT analysis of the experimental generated voltage is given for the developed generator. From the FFT analysis of the generated voltage, %THD of 24.15% is obtained. In this analysis, it is found

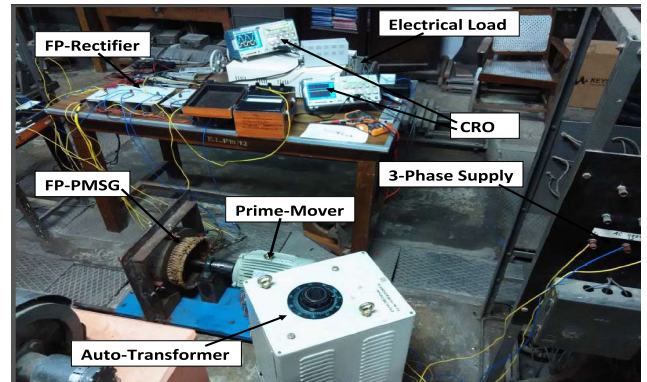


FIGURE 18. Experimental set-up.

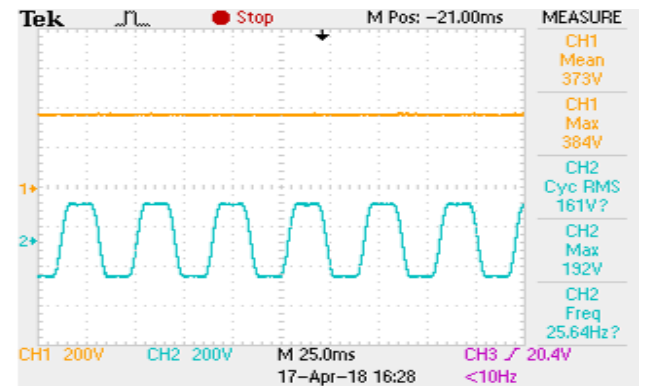


FIGURE 19. Voltage developed at 384.59 rpm.

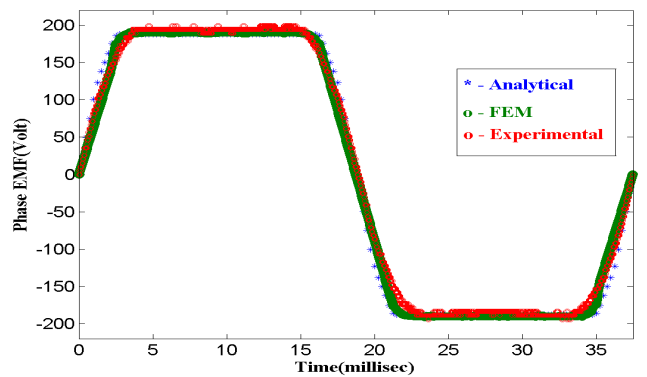


FIGURE 20. Phase voltage comparison for Analytical, FEM and Hardware results.

that, the multiple of fifth order harmonics are absent, whereas other odd harmonics are present. Due to which the shape of the generated voltage is trapezoidal in nature. Fig. 22 shows the generated EMF vs speed characteristics of the developed generator. From this plot, it is clear that the generated voltage obtained from analytical, FEM and experimental with speed are linear in relationship.

The developed FP-PMSG is loaded with resistive load by using five-phase diode rectifier. During loaded condition, the phase terminal voltage is found to be drooping in nature

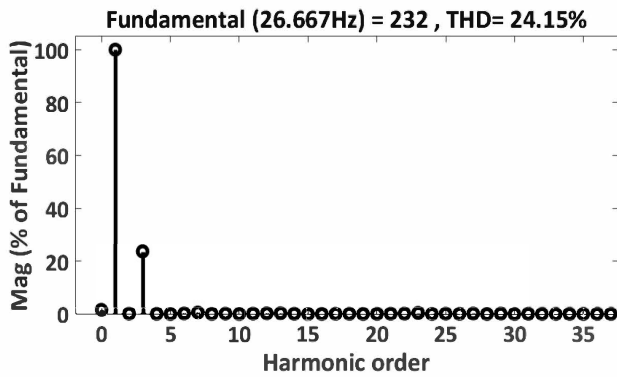


FIGURE 21. FFT Analysis of Generated Voltage.

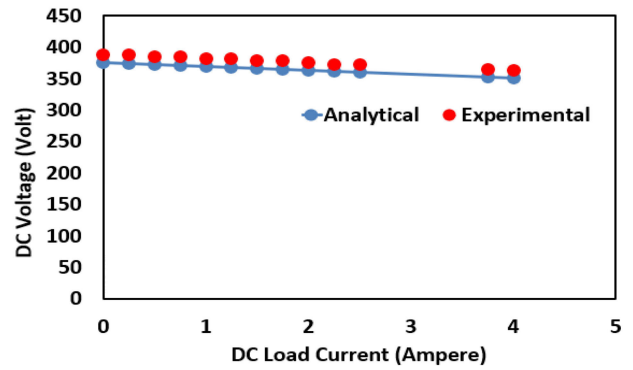


FIGURE 24. DC Voltage vs DC Current.

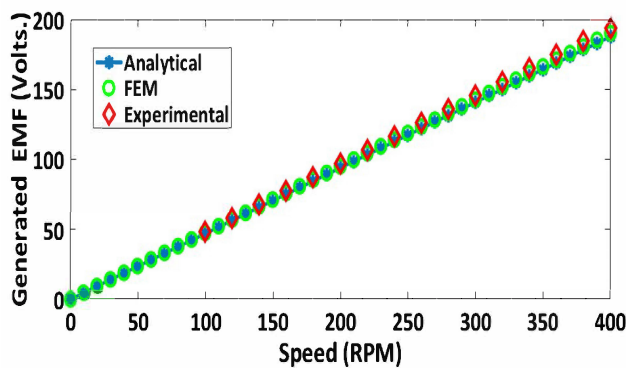


FIGURE 22. Generated EMF Vs Speed.

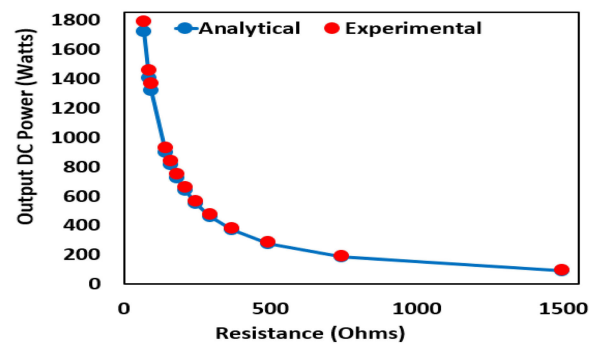


FIGURE 25. Output DC power vs Load resistance.

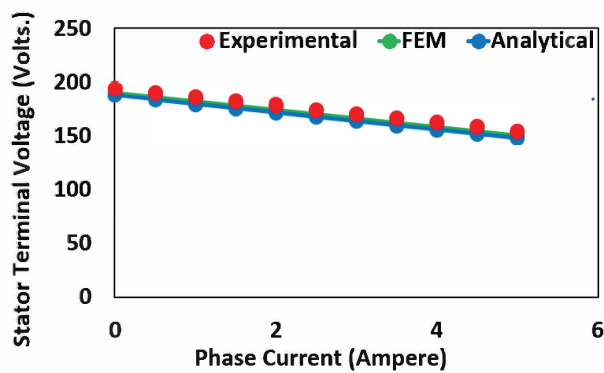


FIGURE 23. Stator Terminal Voltage vs Phase Current.

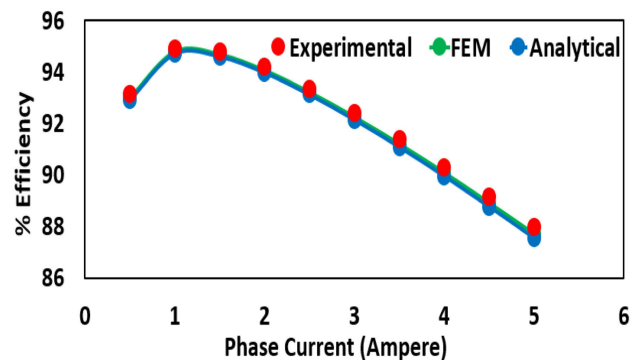


FIGURE 26. % Efficiency vs Phase Current.

as shown in Fig. 23. Due to armature reaction and internal parameters of the generator there is a decrease in the terminal voltage. From the above characteristics, the voltage regulation of analytical, FEM and experimental results are found to be 18.8%, 18.82% and 18.78% respectively. It is concluded that, the voltage regulation of experimental results are better than the other two methods. In Fig. 24, the output of rectified DC voltage vs load current is shown and its characteristic is found to be similar to that of the terminal phase voltage vs phase current. Also, in this plot the analytical voltage is verified with the experimental results and is observed that

both are in close agreement. From the analytical analysis, the analytical rectified DC voltage is found to be 6.58% less than the no load voltage. The variation of the rectified power with to resistive load is carried out, as shown in Fig.25. The experimental findings have been found to be in strong agreement with the analytical results. Further, an efficiency characteristic with phase load current is shown in Fig.26. It is found that at rated load the efficiency is 90.3%, which is the highest value obtained experimentally, whereas, IMC model provides efficiency of 89.95%. The values of efficiency are enlisted in Table 9.

TABLE 9. Analytical, FEM and experimental results.

Parameter	Analytical	FEM	%Diff.1	Experimental	%Diff.2	Unit
Air gap flux density	0.5921	0.5994	1.29	0.5812	2	Tesla
Generated voltage (peak)	187.56	190	1.28	193.92	2	Volts
Terminal Voltage	157.87	159.9	1.28	163.25	2	Volts
% Voltage Regulation	18.8	18.82	0.094	18.78	-0.19	-
Rectified DC Voltage (At no-load)	375.12	-	-	387.84	-	Volts
Rectified DC Voltage	350.4	-	-	363.52	-	Volts
Efficiency (%)	89.95	90.09	0.3878	90.3	0.233	-

In Table 9, the %diff.1 indicates the percentage difference in the magnitude of FEM and analytical result, whereas %diff.2 indicates the percentage difference in the magnitude of experimental and FEM results. The values of %diff.1 and %diff.2 are calculated using (40) and (41) respectively.

% Difference 1 (Diff.1)

$$Diff.1 = \left(\frac{FEM - Analytical}{FEM} \right) * 100 \tag{40}$$

% Difference 2 (Diff.2)

$$Diff.2 = \left(\frac{Experimental - FEM}{Experimental} \right) * 100 \tag{41}$$

Table 10 shows a comparative results over other published works. From the reported values of %diff.1, it can be concluded that, the analytical result of IMC model is more accurate than the results obtained from [24] and [25] with respect to FEM. Similarly, from the reported values of %diff.2, it can be concluded that, the FEM value of proposed model is more accurate than the values obtained from [23] and [26] with respect to experimental results.

TABLE 10. Comparison of Maximum % Differences.

Reference	Parameter	% Diff.1	% Diff.2
[23]	Leakage Flux, Stator and rotor core material and Saturation effect.	-	3.29
[24]	Leakage Flux.	1.3	-
[25]	Armature reaction.	1.67	-
[26]	Stator and rotor core material, Saturation effect and Armature reaction.	-	2
IMC model (Proposed)	Leakage Flux, Stator and rotor core material, Rotor PM sleeve material, Saturation effect and Armature reaction.	1.29	2

VI. CONCLUSION

This paper has highlighted the improved magnetic circuit model for FP-PMSG. It enables to achieve the optimal design and electromagnetic performance in a very short time. From the analytical analysis, it is observed that, the amorphous steel as core material is better because it has high air-gap flux density than the cast iron, air and silicon steel alloy. Similarly, for the rotor PM sleeve the carbon fiber is found to be the most favorable because its electrical conductivity is less than the

other types of sleeve materials such as aluminium, copper and carbon fiber. Also, the carbon fiber PM rotor sleeve limits the generation of eddy current losses in the PM and prevents any chances of demagnetisation of the magnets. At the same time, due to variation in dimensional parameters, such as, height of the permanent magnet, thickness of the rotor PM sleeve and M-M gap, the air gap flux gets affected. It is observed that as the air-gap flux decreases, the generated voltage and the cogging torque also decreases which in turn reduces the magnitude of torque ripple. The IMC model has also been utilised to reveal the adverse effect of core saturation on air-gap flux density distribution. For the validation of analytical and FEM results, prototype has been developed. During the development of the prototype, the difficulties faced in the laboratory have also been discussed. The results such as airgap field density, generated voltage, generated voltage vs speed, terminal voltage vs current, %voltage regulation, rectified DC Voltage vs DC current and %efficiency vs current are compared and the difference is found within 2%. By the fabrication process of the prototype of FP-PMSG in laboratory, enormous values of engineering design and construction has been learnt.

REFERENCES

- [1] J. Stuyts, G. Horn, W. Vandermeulen, J. Driesen, and M. Diehl, "Effect of the electrical energy conversion on optimal cycles for pumping airborne wind energy," *IEEE Trans. Sustain. Energy*, vol. 6, no. 1, pp. 2–10, Jan. 2015.
- [2] R. M. Elavarasan, G. M. Shafiullah, S. Padmanaban, N. M. Kumar, A. Annam, A. M. Vetrichelvan, L. Mihet-Popa, and J. B. Holm-Nielsen, "A comprehensive review on renewable energy development, challenges, and policies of leading Indian states with an international perspective," *IEEE Access*, vol. 8, pp. 74432–74457, 2020.
- [3] B. S. Pali and S. Vadhera, "An innovative continuous power generation system comprising of wind energy along with pumped-hydro storage and open well," *IEEE Trans. Sustain. Energy*, vol. 11, no. 1, pp. 145–153, Jan. 2020.
- [4] W. Zhang and K. Fang, "Controlling active power of wind farms to participate in load frequency control of power systems," *IET Gener., Transmiss. Distrib.*, vol. 11, no. 9, pp. 2194–2203, Jun. 2017.
- [5] M. H. Qais, H. M. Hasanien, and S. Alghuwainem, "A grey wolf optimizer for optimum parameters of multiple PI controllers of a grid-connected PMSG driven by variable speed wind turbine," *IEEE Access*, vol. 6, pp. 44120–44128, 2018.
- [6] J. Ouyang, M. Li, Y. Diao, T. Tang, and Q. Xie, "Active control method of large-scale wind integrated power system with enhanced reactive power support for wind speed fluctuation," *IET Gener., Transmiss. Distrib.*, vol. 12, no. 21, pp. 5664–5671, Nov. 2018.
- [7] M. H. Qais, H. M. Hasanien, and S. Alghuwainem, "Low voltage ride-through capability enhancement of grid-connected permanent magnet synchronous generator driven directly by variable speed wind turbine: A review," *J. Eng.*, vol. 2017, no. 13, pp. 1750–1754, Jan. 2017.
- [8] M. Rajvikram, P. Renuga, and M. Swathisriranjani, "Fuzzy based MPPT controller's role in extraction of maximum power in wind energy conversion system," in *Proc. Int. Conf. Control, Instrum., Commun. Comput. Technol. (ICCICCT)*, Dec. 2016, pp. 713–719.
- [9] M. Abdelrahem, C. M. Hackl, Z. Zhang, and R. Kennel, "Robust predictive control for direct-driven surface-mounted permanent-magnet synchronous generators without mechanical sensors," *IEEE Trans. Energy Convers.*, vol. 33, no. 1, pp. 179–189, Mar. 2018.
- [10] M. A. S. Ali, K. K. Mehmood, S. Baloch, and C.-H. Kim, "Wind-speed estimation and sensorless control for SPMSG-based WECS using LMI-based SMC," *IEEE Access*, vol. 8, pp. 26524–26535, 2020.
- [11] L. Trilla, O. Gomis-Bellmunt, and F. D. Bianchi, "Linear parameter-varying control of permanent magnet synchronous generators for wind power systems," *World Acad. Sci., Eng. Technol., Int. J. Energy Power Eng.*, vol. 7, no. 3, pp. 692–704, Mar. 2014.

- [12] M. Rajvikram, P. Renuga, G. A. Kumar, and K. Bavithra, "Fault ride-through capability of Permanent Magnet Synchronous Generator based Wind Energy Conversion System," *Power Res.*, vol. 12, pp. 531–538, 2016.
- [13] M. Polikarpova, P. Ponomarev, P. R oytt , S. Semken, Y. Alexandrova, and J. Pyrh onen, "Direct liquid cooling for an outer-rotor direct-drive permanent-magnet synchronous generator for wind farm applications," *IET Electr. Power Appl.*, vol. 9, no. 8, pp. 523–532, Sep. 2015.
- [14] V. Yaramasu, A. Dekka, M. J. Dur n, S. Kouro, and B. Wu, "PMSG-based wind energy conversion systems: Survey on power converters and controls," *IET Electr. Power Appl.*, vol. 11, no. 6, pp. 956–968, Jul. 2017.
- [15] C. Xue, W. Song, and X. Feng, "Finite control-set model predictive current control of five-phase permanent-magnet synchronous machine based on virtual voltage vectors," *IET Electr. Power Appl.*, vol. 11, no. 5, pp. 836–846, May 2017.
- [16] R. R. Kumar, S. K. Singh, R. K. Srivastava, and R. K. Saket, "Dynamic reluctance air gap modeling and experimental evaluation of electromagnetic characteristics of five-phase permanent magnet synchronous generator for wind power application," *Ain Shams Eng. J.*, vol. 11, no. 2, pp. 377–387, Jun. 2020.
- [17] N. K. Nguyen, F. Meinguet, E. Semail, and X. Kestelyn, "Fault-tolerant operation of an open-end winding five-phase PMSM drive with short-circuit inverter fault," *IEEE Trans. Ind. Electron.*, vol. 63, no. 1, pp. 595–605, Jan. 2016.
- [18] Y. Chen and B. Liu, "Design and analysis of a five-phase fault-tolerant permanent magnet synchronous motor for aerospace starter-generator system," *IEEE Access*, vol. 7, pp. 135040–135049, 2019.
- [19] R. R. Kumar, P. Devi, C. Chetri, A. S. S. Vardhan, R. M. Elavarasan, L. Mihet-Popa, and R. K. Saket, "Design and characteristics investigation of novel dual stator pseudo-pole five-phase permanent magnet synchronous generator for wind power application," *IEEE Access*, vol. 8, pp. 175788–175804, 2020.
- [20] C. Xiong, H. Xu, T. Guan, and P. Zhou, "A constant switching frequency Multiple-Vector-Based model predictive current control of five-phase PMSM with nonsinusoidal back EMF," *IEEE Trans. Ind. Electron.*, vol. 67, no. 3, pp. 1695–1707, Mar. 2020.
- [21] G. Feng, C. Lai, W. Li, J. Tjong, and N. C. Kar, "Open-phase fault modeling and optimized fault-tolerant control of dual three-phase permanent magnet synchronous machines," *IEEE Trans. Power Electron.*, vol. 34, no. 11, pp. 11116–11127, Nov. 2019.
- [22] S. M. Raziee, O. Misir, and B. Ponick, "Winding function approach for winding analysis," *IEEE Trans. Magn.*, vol. 53, no. 10, pp. 1–8, Jun. 2017.
- [23] D.-K. Lim and J.-S. Ro, "Analysis and design of a delta-type interior permanent magnet synchronous generator by using an analytic method," *IEEE Access*, vol. 7, pp. 85139–85145, 2019.
- [24] H.-K. Yeo, D.-K. Lim, and H.-K. Jung, "Magnetic equivalent circuit model considering the overhang structure of an interior permanent-magnet machine," *IEEE Trans. Magn.*, vol. 55, no. 6, pp. 1–4, Jun. 2019.
- [25] X. Zhang, C. Zhang, J. Yu, P. Du, and L. Li, "Analytical model of magnetic field of a permanent magnet synchronous motor with a trapezoidal Halbach permanent magnet array," *IEEE Trans. Magn.*, vol. 55, no. 7, pp. 1–5, Jul. 2019.
- [26] C. He and T. Wu, "Analysis and design of surface permanent magnet synchronous motor and generator," *CES Trans. Electr. Mach. Syst.*, vol. 3, no. 1, pp. 94–100, 2019.
- [27] R. Kolano, A. Kolano-Burian, K. Krykowski, J. Hetmanczyk, M. Hreczka, M. Polak, and J. Szynowski, "Amorphous soft magnetic core for the stator of the high-speed PMBLDC motor with half-open slots," *IEEE Trans. Magn.*, vol. 52, no. 6, pp. 1–5, Jun. 2016.
- [28] Y. Kong, M. Lin, R. Guo, N. Li, and D. Xu, "Design and optimization of outer-rotor permanent magnet synchronous machine with amorphous stator core," *IEEE Trans. Appl. Supercond.*, vol. 28, no. 3, pp. 1–4, 2018.
- [29] J. H. Kim, C. J. Hyeon, S. H. Chae, D. J. Kim, C.-J. Boo, Y.-S. Jo, Y. S. Yoon, S.-G. Kim, H. Lee, and H. M. Kim, "Design and analysis of cooling structure on advanced air-core stator for megawatt-class HTS synchronous motor," *IEEE Trans. Appl. Supercond.*, vol. 27, no. 4, pp. 1–7, Jun. 2017.
- [30] H. Fang, D. Li, R. Qu, J. Li, C. Wang, and B. Song, "Rotor design and eddy-current loss suppression for high-speed machines with a solid-PM rotor," *IEEE Trans. Ind. Appl.*, vol. 55, no. 1, pp. 448–457, Jan. 2019.
- [31] J.-H. Ahn, C. Han, C.-W. Kim, and J.-Y. Choi, "Rotor design of high-speed permanent magnet synchronous motors considering rotor magnet and sleeve materials," *IEEE Trans. Appl. Supercond.*, vol. 28, no. 3, pp. 1–4, Apr. 2018.
- [32] V. Behjat and M. Hamrahi, "Dynamic modeling and performance evaluation of axial flux PMSG based wind turbine system with MPPT control," *Ain Shams Eng. J.*, vol. 5, no. 4, pp. 1157–1166, Dec. 2014.
- [33] D. C. Hanselman, *Brushless Permanent-Magnet Motor Design*. New York, NY, USA: McGraw-Hill, 1994.



RAJA RAM KUMAR (Student Member, IEEE) received the B.Tech. degree in electrical engineering from the West Bengal University of Technology, Kolkata, India, in 2010, and the M.Tech. and Ph.D. degrees in electrical machines and drives from the Indian Institute of Technology (BHU) Varanasi, Varanasi, India, in 2012 and 2018, respectively. He is currently working as an Assistant Professor with the Department of Electrical Engineering, Jorhat Engineering College, Assam.

He is the author of several research articles, which are published in international/national journals and conference proceedings. His current research interests include renewable energy, electrical machines, electric drives, as well as power electronic converter design and control. He received the Institute Research Award from IIT (BHU) Varanasi, in 2016, and the second prize Paper Award in IACC Annual Meeting 2018 at Portland during IAS Annual Meeting. He was the Chair-Person of the Student Branch of the IEEE-IAS at IIT (BHU) Varanasi, from 2016 to 2018.



SANTOSH K. SINGH (Senior Member, IEEE) received the bachelor's degree in electrical engineering from Madan Mohan Malaviya University of Technology (MMMUT), Gorakhpur, India, in 2000, the master's degree in power electronics electrical machine and drives from IIT Delhi, India, in 2001, and the Ph.D. degree from the Electrical Engineering Division, University of Cambridge, U.K., in 2011. His Ph.D. work was focused on Silicon Carbide (SiC)-based Inverter

for hybrid electric vehicles.

From 2002 to 2005, he was Lecturer at GCET, Greater Noida, India. Since 2005, he has been with the Indian Institute of Technology (BHU) Varanasi, Varanasi, India, where he is currently working as an Associate Professor with the Department of Electrical Engineering. His research interests include power electronic topologies and their control, silicon carbide converters, and electric machine and drives. The focus of his current research is on magnetically coupled dual stator permanent magnet synchronous generator, high gain hybrid converters with peculiar NZ-DCM phenomena, high gain ac-ac matrix converter, gate drive circuit for SiC devices, and low device count multilevel inverters. He is currently working on a research project entitled "Prospects of power converters for Integration of Electric vehicle charging stations with the existing Electric distribution system in India" in collaboration with the University of Warwick and the University of Cambridge, U.K.

Dr. Singh is a member of the IET, and a Life Member of IEI, India, and ISTE. He chaired sessions in PEDES 2016, UPCON 2016, ECCE 2017, and PEDES 2018 conferences of the IEEE. In 2018, his research team was awarded the Second Prize Paper Award from the IEEE the Industry Applications Society. He is an active Reviewer of the IEEE TRANSACTION IN POWER ELECTRONICS, IEEE TRANSACTION IN INDUSTRIAL ELECTRONICS, and *Journal of Emerging Technologies*.



R. K. SRIVASTAVA (Senior Member, IEEE) received the B.Tech. degree in electrical engineering, the M.Tech. degree in electrical machines and drives, and the Ph.D. degree in electrical machines from the erstwhile Institute of Technology, Banaras Hindu University, Varanasi, India, in 1983, 1985, and 2000, respectively. He is currently working as a Professor in Electrical Machines and Drives. He has published several research articles in international/national journals and conference proceedings. He has authored two books. His specializations are the electromagnetic field applied to electrical machines, linear induction machines, special purpose electrical machines, permanent magnets motors and generators, and Eddy current brake. Prof. Srivastava was a Convener of the International Conference IEEE Uttar Pradesh Section: International Conference on Electrical, Computer, and Electronics (UPCON-2016), IIT (BHU) Varanasi. He is an Adviser and Founder of the IEEE Industry Applications Society Student Chapter at IIT (BHU) Varanasi.



AKANKSHA SINGH S. VARDHAN received the B.Tech. degree in electrical engineering from the Sam Higginbottom University of Agriculture, Technology and Sciences, Allahabad, India, in 2019. She is currently pursuing the M.E. degree in electrical engineering, specializing in power electronics, with Shri G.S. Institute of Technology and Science, Indore, India, affiliated to the Rajiv Gandhi University of Technology, Bhopal, India. Her innovative research work entitled “Movable Solar Power Generator” has been nominated for the prestigious GYTI Award—2020 at Rashtrapati Bhavan, New Delhi, India. She has published many research articles in reputed international journals and conference proceedings. Her research interests include power electronics and drives, renewable energy technology, SEIG and DFIG controller design, synchronous generator modeling, reliability engineering, and green energy conversion systems.



RAJVIKRAM MADURAI ELAVARASAN received the B.E. degree in electrical and electronics engineering from Anna University, Chennai, India, and the M.E. degree in power system engineering from Thiagarajar College of Engineering, Madurai. He was a gold medalist of the master's degree. He worked as an Associate in Technical Operations at the IBM Global Technology Services Division, and as an Assistant Professor with the Department of Electrical and Electronics Engineering, Sri Venkateswara College of Engineering, Chennai. He currently works as a Design Engineer with the Electrical and Automotive Parts Manufacturing Unit, AA Industries, Chennai. He has published articles in international journals, as well as international and national conferences. His areas of interest include solar PV cooling techniques, renewable energy and smart grids, wind energy research, power system operation and control, artificial intelligence, control techniques, and demand-side management. He is a recognized reviewer in reputed journals namely IEEE SYSTEMS, IEEE ACCESS, IEEE Communications Magazine, International Transactions on Electrical Energy Systems (Wiley), Energy Sources, Part A: Recovery, Utilization and Environmental Effects (Taylor and Francis), Scientific Reports (Springer Nature), Chemical Engineering Journal (Elsevier), and CFD Letters and 3 Biotech (Springer).



R. K. SAKET (Senior Member, IEEE) is currently with the Department of Electrical Engineering, Indian Institute of Technology (BHU) Varanasi, India. He has more than 20 years of academic and research experience. He is the author/coauthor of approximately 110 scientific articles, book chapters, and research articles in prestigious international journals and conference proceedings. His research interests include power system reliability, electrical machines and drives, reliability engineering, induction generators, DFIG controller design, and renewable energy systems. He is a Fellow of the Institution of Engineers (India), and a member of the IET, U.K. He is an Associate Editor of the *IET – Renewable Power Generation*, U.K., and an Editorial Board Member of the *Engineering, Technology & Applied Science Research*, Greece, and the *Journal of Electrical Systems*, France. He has received many awards, honors, and recognition for his academic and research contributions, including the prestigious GYTI Award–2018 by the Hon'ble President of India at New Delhi, India; Design Impact Award–2018 by Padma Vibhushan Ratan Tata at Mumbai, India; and Nehru Encouragement Award by M.P. State Government, Bhopal, India.



EKLAS HOSSAIN (Senior Member, IEEE) received the B.S. degree in electrical and electronic engineering from the Khulna University of Engineering and Technology, Bangladesh, in 2006, the M.S. degree in mechatronics and robotics engineering from the International Islamic University of Malaysia, Malaysia, in 2010, and the Ph.D. degree from the College of Engineering and Applied Science, University of Wisconsin Milwaukee (UWM).

He has been involved with several research projects on renewable energy and grid-tied microgrid system at Oregon Tech, as an Assistant Professor with the Department of Electrical Engineering and Renewable Energy, since 2015. He is currently working as an Associate Researcher with the Oregon Renewable Energy Center (OREC). He, along with his dedicated research team, is looking forward to explore methods to make the electric power systems more sustainable, cost-effective, and secure through extensive research and analysis on energy storage, microgrid systems, and renewable energy sources. He is also the Certified Energy Manager (CEM) and a Renewable Energy Professional (REP). He has also been working in the area of distributed power systems and renewable energy integration, for the last ten years. He has published a number of research articles and posters in this field. His research interests include modeling, analysis, design, and control of power electronic devices, energy storage systems, renewable energy sources, integration of distributed generation systems, microgrid and smart grid applications, robotics, and advanced control systems. He is a Senior Member of the Association of Energy Engineers (AEE). He is also the winner of the Rising Faculty Scholar Award (2019) from the Oregon Institute of Technology, for his outstanding contribution in teaching. He is also serving as an Associate Editor for IEEE Access. He is also a registered Professional Engineer (PE) of Oregon, USA.

...